RESEARCH ARTICLE
PLANETARY SCIENCES

Earth and Planetary Physics
8: 459–471, 2024
doi: 10.26464/epp2024028

The anisotropy of suprathermal electrons in the Martian ionosphere

YuTian Cao[1,2], Jun Cui[1,3*], XiaoShu Wu[1,3], WenJun Liang[1], RuiQi Fu[1], and HaoYu Lu[4]

[1]Planetary Environmental and Astrobiological Research Laboratory (PEARL), School of Atmospheric Sciences, Sun Yat-sen University, Zhuhai 519082, China;

[2]Key Laboratory of Geospace Environment, University of Science & Technology of China, Chinese Academy of Sciences, Hefei 230026, China;

[3]Center for Excellence in Comparative Planetology, Chinese Academy of Sciences, Hefei 230026, China;

[4]School of Space and Environment, Beihang University, Beijing 102206, China

Key Points:

- We investigate the pitch angle distribution of suprathermal electrons in the Martian ionosphere using the MAVEN SWEA measurements.
- The anisotropy of suprathermal electrons is energy dependent, magnetically controlled, and shows clear altitudinal and diurnal variations.
- The observations reflect the combined result of photoelectrons which are near isotropic and SW electrons which are highly anisotropic.

Citation: Cao, Y. T., Cui, J., Wu, X. S., Liang, W. J., Fu, R. Q., and Lu, H. Y. (2024). The anisotropy of suprathermal electrons in the Martian ionosphere. *Earth Planet. Phys.*, *8*(3), 459–471. http://doi.org/10.26464/epp2024028

Abstract: Suprathermal electrons are an important population of the Martian ionosphere, either produced by photoionization of atmospheric neutrals or supplied from the Solar Wind (SW). This study is dedicated to an in-depth investigation of the pitch angle distribution of suprathermal electrons at two representative energies, 19–55 eV and 124–356 eV, using the extensive measurements made by the Solar Wind Electron Analyzer on board the Mars Atmosphere and Volatile Evolution. Throughout the study, we focus on the overall degree of anisotropy, defined as the standard deviation of suprathermal electron intensity among different directions which is normalized by the mean omni-directional intensity. The available data reveal the following characteristics: (1) In general, low energy electrons are more isotropic than high energy electrons, and dayside electrons are more isotropic than nightside electrons; (2) On the dayside, the anisotropy increases with increasing altitude at low energies but remains roughly constant at high energies, whereas on the nightside, the anisotropy decreases with increasing altitude at all energies; (3) Electrons tend to be more isotropic in strongly magnetized regions than in weakly magnetized regions, especially on the nightside. These observations indicate that the anisotropy is a useful diagnostic of suprathermal electron transport, for which the conversion between the parallel and perpendicular momenta as required by the conservation of the first adiabatic invariant, along with the atmospheric absorption at low altitudes, are two crucial factors modulating the observed variation of the anisotropy. Our analysis also highlights the different roles on the observed anisotropy exerted by suprathermal electrons of different origins.

Keywords: Mars; ionosphere; suprathermal electron; pitch angle distribution

1. Introduction

Unlike the Earth, Mars lacks a global dynamo magnetic field and thus its upper atmosphere and ionosphere interact directly with the Solar Wind (SW) (Nagy et al., 2004). Suprathermal electrons (1–1000 eV) are an important composition of the Martian ionosphere, often used as a diagnostic of the ambient magnetic field topology because these electrons are typically magnetized and propagate along the magnetic field lines above the suprathermal electron exobase (e.g. Xu SS et al., 2015; 2016a). Existing measurements of suprathermal electrons have revealed an extremely complicated magnetic field topology near Mars, including both the contribution from an induced magnetosphere and the contribution from crustal magnetic anomalies known to cluster over the southern hemisphere of the planet (e.g. Xu SS et al., 2017a, b; 2019).

Suprathermal electrons consist of photoelectrons and SW electrons. Photoelectrons are produced by solar Extreme Ultraviolet (EUV) and X-ray ionization of various neutrals in the dayside Martian upper atmosphere (e.g. Fox et al., 2008; Coates et al., 2011). A typical photoelectron energy spectrum observed at Mars is characterized by several distinctive peaks at 22–27 eV related to the He II 30.4 nm line, which is the most intensive EUV emission line in the solar spectrum capable of ionizing atmospheric neutrals such as CO_2 and Os (e.g. Frahm et al., 2006a, b). In addition, the rapid drop in solar radiation at wavelengths shorter than

First author: Y. T. Cao, caoyt6@mail.sysu.edu.cn
Correspondence to: J. Cui, cuijun7@mail.sysu.edu.cn
Received 19 FEB 2024; Accepted 02 APR 2024.
First Published online 24 APR 2024.

17 nm produces a pronounced knee around 60−70 eV in the photoelectron energy spectrum (e.g. Sakai et al., 2015; Peterson et al., 2016). These spectral features have been observed by various instruments over the past four decades (e.g. Mantas and Hanson, 1979; Frahm et al., 2006b; Sakai et al., 2015; Peterson et al., 2016). The peaks at 22−27 eV are the most extensively studied feature of the photoelectron energy distribution and have been frequently used to identify the ambient magnetic field topology (e.g. Liemohn et al., 2006; Frahm et al., 2006a; Xu SS et al., 2017a, b; 2019; Cao YT et al., 2021). Meanwhile, it has been shown that other characteristics of the photoelectron energy distribution also contain important information on the background atmosphere. For instance, Wu XS et al. (2019a) found that the shape of the photoelectron intensity at 10−50 eV is a diagnostic of the inelastic collisions between photoelectrons and atmospheric neutrals. In another study, Wu XS et al. (2020b) further investigated the altitudinal variation of photoelectron intensity and proposed that the intensity at 10−15 eV was a good indicator of the ambient atmospheric composition.

Properties of SW electrons are usually studied on the nightside of Mars because the precipitation of these energetic electrons is thought to be the dominant source driving atmospheric and ionospheric variability in the darkness (e.g. Verigin et al., 1991; Safaeinili et al., 2007; Fowler et al., 2015; Girazian et al., 2017; Adams et al., 2018; Lillis et al., 2018). Based on a comparison between the SW electron impact ionization rate and dissociative recombination rate on the deep nightside of Mars, Cui J et al. (2019) proposed that below a certain altitude, electron precipitation was able to fully account for the nightside ionospheric observations and extra sources were not required. The SW dynamical pressure has been suggested as an important factor controlling plasma formation via impact ionization in the deep nightside Martian upper atmosphere (e.g. Lillis and Brain, 2013; Lillis et al., 2018; Xu SS et al., 2016b). Besides, several studies have revealed that nightside SW electron precipitation is substantially reduced near strong crustal magnetic anomalies, which is, in the extreme situation, manifest as suprathermal electron depletions frequently observed on the nightside of Mars (e.g. Steckiewicz et al., 2015, 2017; Niu DD et al., 2020).

The pitch angle distribution (PAD) provides key information to characterize suprathermal electrons, where the pitch angle is defined as the angle between the electron velocity and ambient magnetic field direction, with 0° and 180° representing electrons traveling parallel and anti-parallel to the ambient magnetic field lines. For instance, Xu SS et al. (2019) combined two independent methods based on both the PAD and energy distribution of suprathermal electrons and identified seven categories of magnetic topology in the Martian ionosphere. Previous studies of the suprathermal electron PAD usually focused on electrons with a typical energy of several hundred eV, thus mainly characterizing SW electrons (e.g. Weber et al., 2017; Xu SS et al., 2019). The photoelectron PAD has been recently examined by Cao YT et al. (2021) and shown to be nearly isotropic on the dayside but field-aligned on the nightside. However, Shane et al. (2019) presented a model-data comparison in Martian dayside-closed crustal magnetic field regions for low energy electrons (10−60 eV) and high energy electrons (100−500 eV), respectively. The work reported that the low energy electron had PAD in agreement with the suprathermal electron transport model, while high energy electrons do not. Such a result strongly suggests that the PAD of suprathermal electrons at different energies varies differently and should be studied simultaneously.

The present study is devoted to a systematic and comparative investigation of the PAD of suprathermal electrons at different energies, representing either photoelectrons or SW electrons. We describe in Section 2 the data set used, from which we derive the standard deviation (STD) of the observed differential intensities of suprathermal electrons along different directions to categorize their PAD. The broad characteristics of the PAD, in terms of the degree of anisotropy, are presented in Section 3, highlighting the differences between suprathermal electrons at different energies. This is followed by Section 4 where we focus on the variations of the suprathermal electron anisotropy with altitude, solar zenith angle (SZA), magnetic field configuration, solar activity, as well as upstream SW condition. Finally, we discuss in Section 5 and draw conclusions in Section 6. Throughout the study, a simple parameter easily extracted from the data is used to characterize the overall degree of suprathermal electron anisotropy, irrespective of the detailed shape of the measured PAD. We also emphasize that it is necessary to explore the variations of such a parameter at different energies to fully characterize the complex plasma environment near Mars and distinguish between suprathermal electrons of different origins.

2. Data Set and Methodology

Our analysis is based on the differential suprathermal electron intensity measurements made by the Solar Wind Electron Analyzer (SWEA) on board the Mars Atmosphere and Volatile Evolution (MAVEN) spacecraft from 18 October 2014 to 14 May 2019 (Mitchell et al., 2016). The SWEA is a symmetric hemispheric electrostatic analyzer that measures the differential intensity of suprathermal electrons over the energy range of 3 eV to 4.6 keV with a resolution of 17% and the range of incoming direction covering a field of view (FOV) of 360° × 120° of which 8% is blocked by the spacecraft body. Because of the limited energy resolution, the SWEA cannot distinguish among multiple photoelectron energy peaks at 22−27 eV. The suprathermal electron PAD is determined by combining the SWEA data and the magnetic field data acquired by the MAVEN Magnetometer (MAG) (Connerney et al., 2015). The SWEA electron PAD is comprised of sixteen 22.5° wide pitch angle bins which are formed every instrument energy sweep by a combination of measurements which change depending on the local magnetic field orientation. Because the 16 PAD bins span 360° in azimuth, the PAD is measured twice (Mitchell et al., 2016) and all these 16 measurements are used in this study.

For the purpose of this study, we determine the integrated intensities of suprathermal electrons, in units of cm^{-2} s^{-1} sr^{-1}, over the energy range of 19−55 eV, which are classified as the low energy electrons. As discussed in Section 1, electrons with energy less than 70 eV are usually used to characterize photoelectrons produced via photoionization (e.g. Wu XS et al., 2019a; Cao YT

et al., 2021). The integrated intensities at different pitch angles are calculated independently and normalized by the average integrated intensity. We then derive the standard deviation of these normalized integrated intensities, defined as

$$\mathrm{STD} = \sqrt{\sum_{i=1}^{n}(I_i - \bar{I})^2/(n-1)},$$

where I_i is the normalized integrated intensity measured in the i_{th} pitch angle bin and $\bar{I}$ is the intensity averaged over all bins, which equals to 1 due to the normalization. The STD is used as a diagnostic of the anisotropy of the suprathermal electron distribution, with a smaller STD representing a more isotropic PAD. Because electrons with hundreds eV have been used to characterize the Martian magnetic topology in several studies (e.g. Weber et al., 2017; Xu SS et al., 2019), we calculate similarly the STD of the normalized integrated intensities for suprathermal electrons at 124−356 eV, which are classified as the high energy electrons in our subsequent analyses. This energy range includes 10 SWEA energy channels, which is consistent with the number of energy channels used for energy range of 19−55 eV. As detailed below, these two energy ranges, with distinct characteristics of the observed PAD, are chosen to represent either photoelectrons or SW electrons. Throughout the rest of the paper, the STD determined for each SWEA energy spectrum is referred to as the anisotropic factor or anisotropy for short.

As an example, we show in Figure 1 the PAD of low and high energy electrons measured during MAVEN orbit #1082 on 21 April 2015. During this orbit, the spacecraft passed by a periapsis altitude of 130 km at a Universal Time (UT) of 12:47:12. We present in the figure the suprathermal electron energy spectra measured from 12:37:38 UT to 12:57:38 UT when the spacecraft moved between ~430 km and the periapsis during the inbound and outbound portion of the orbit and stayed completely on the dayside. The omni-directional suprathermal electron intensity, defined as the intensity averaged over all available pitch angles, is presented in panel (a) as a function of time, whereas the PADs of low and high energy electrons are displayed in panels (b) and (c), respectively. Panel (d) shows the variations of the altitude (blue) and SZA (red) at the spacecraft location. Panel (e) shows the ambient magnetic field intensity (blue) measured by the MAG and the corresponding magnetic field elevation angle (red) with 0° representing a strictly horizontal magnetic field relative to the surface of Mars. Panel (f) shows the anisotropic factors for low (red) and high (blue) energy electrons. Some PADs and the corresponding anisotropic factors are left blank due to lack of valid data in one or more pitch angle bins.

Before 12:50:10 UT, the low energy electrons were isotropic with an average anisotropic factor of 0.08 only. Between 12:50:40 UT and 12:53:38 UT, the low energy electrons were still near isotropic

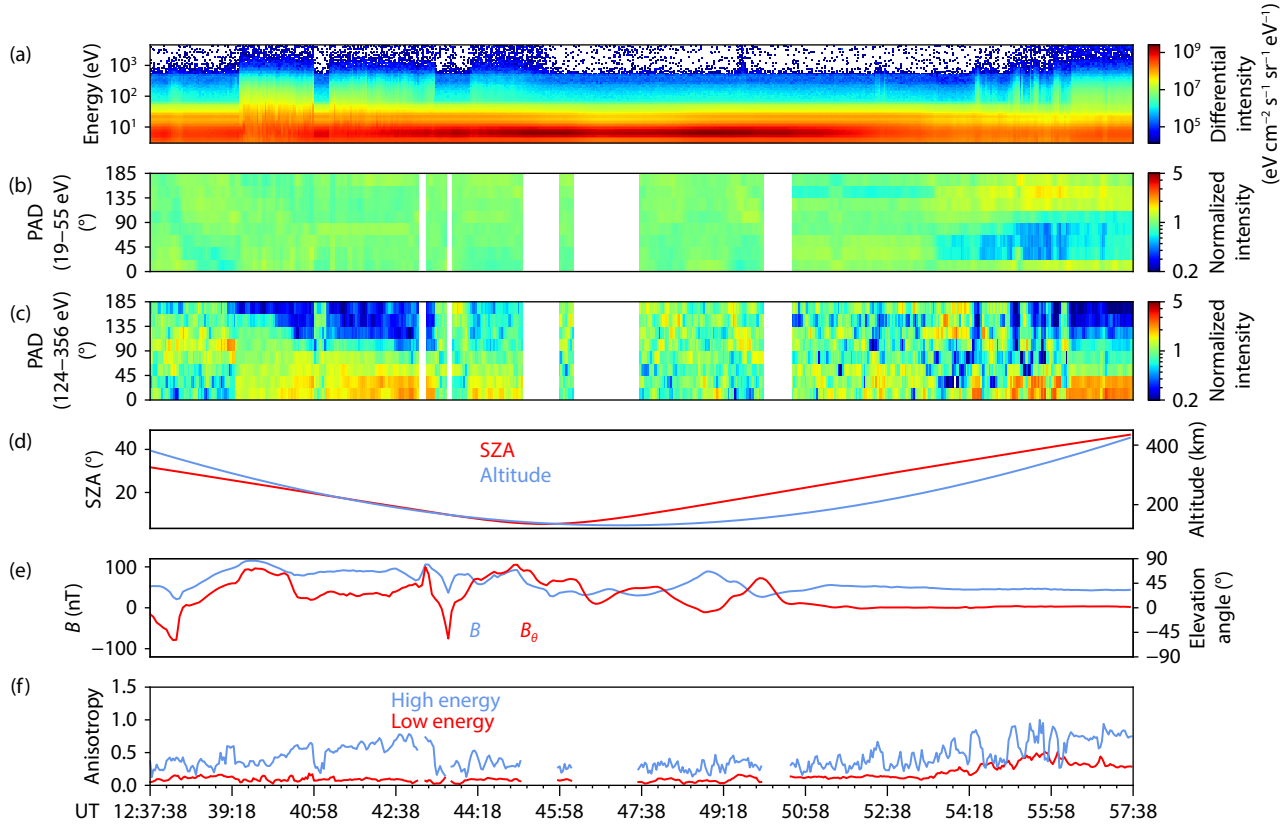

Figure 1. The SWEA suprathermal electron energy spectra measured during MAVEN orbit #1082 on 21 April 2015. (a) The omni-directional electron intensity averaged over all pitch angles; (b) The normalized integrated intensity of low energy electrons at 19−55 eV; (c) Similar to panel (b) but for high energy electrons at 124−356 eV; (d) The altitude and SZA at the spacecraft location; (e) The ambient magnetic field intensity and the correspond magnetic field elevation angle measured by the MAG; (f) The anisotropic factors for low (red) and high (blue) energy electrons derived from the spectra in panels (b) and (c).

though the average anisotropic factor increased to 0.12. Before 12:53:38 UT, the photoelectron energy peak at 22−27 eV was prominent in panel (a), indicating the dominant source of the measured photoelectrons. After 12:53:38 UT when the spacecraft ascended above 250 km, the low energy electrons became anisotropic and the anti-parallel intensity was roughly two times the parallel intensity with an average anisotropic factor of 0.32. The photoelectron peaks became faded with increasing altitude and disappeared after 12:55:58 UT. However, the PAD of high energy electrons in Figure 1 is quite different from that of low energy electrons. For the bulk of the displayed time interval, the high energy electrons were strongly anisotropic with the pitch angle of maximum intensity varying in a random fashion for most of the time. Between 12:39:38 UT and 12:43:18 UT and after 12:56:18 UT, the the high energy electrons showed an ordered fashion with the parallel intensity substantially enhanced over the anti-parallel intensity. During this time interval, the anisotropic factor of high energy electrons varied between 0.12 and 0.94, with an average value of 0.42

In Figure 2, we show another example for MAVEN orbit #475 on 27 December 2014, during which the spacecraft passed by a periapsis altitude of 153 km at 18:04:23 UT. We show in the figure the suprathermal electron energy spectra measured from 17:54:45 UT to 18:14:45 UT when the spacecraft flew from the nightside to the dayside during the outbound portion of its orbit. Before 18:09:51 UT, both low and high energy electrons were strongly anisotropic, showing the analogous PAD patterns and the anti-parallel intensity was more than three times greater than the parallel intensity. During this time, the spacecraft was beyond the EUV terminator indicated by the green line in panel (d) adapted from Lillis et al. (2018), implying that the spacecraft was in the darkness. Between 18:09:51 UT and 18:12:33 UT, the spacecraft crossed the EUV terminator from the nightside to the dayside, during which the anti-parallel intensity of high energy electrons was greater than the respective parallel intensity, whereas the anti-parallel intensity of low energy electrons was in contrast smaller than the parallel intensity. Between 18:12:33 UT and 18:14:15 UT, the low energy electrons were near isotropic with an average anisotropic factor of 0.16, but the PAD of high energy electrons remained similar to early times. With increasing altitude, both the low and high energy electrons became strongly anisotropic after 18:14:15 UT. The photoelectron energy peak is kept invisible in panel (a) throughout the measurements.

For both examples, the PADs of electrons at different energies are quite different in either the direction of maximum intensity or the degree of anisotropy. Two interesting features are revealed by the data: (1) high energy electrons are more anisotropic than low energy electrons except in limited situations such as over the time interval of 18:09:51 UT to 18:12:33 UT during orbit #475; (2) the PAD of low energy electrons appears to be fairly stable on the dayside but varies over timescales much shorter than 1 min on the nightside, to be distinguished from the PAD of high energy electrons which varies rapidly on both sides. In practice, these two features are commonly seen in the SWEA energy spectra. Both

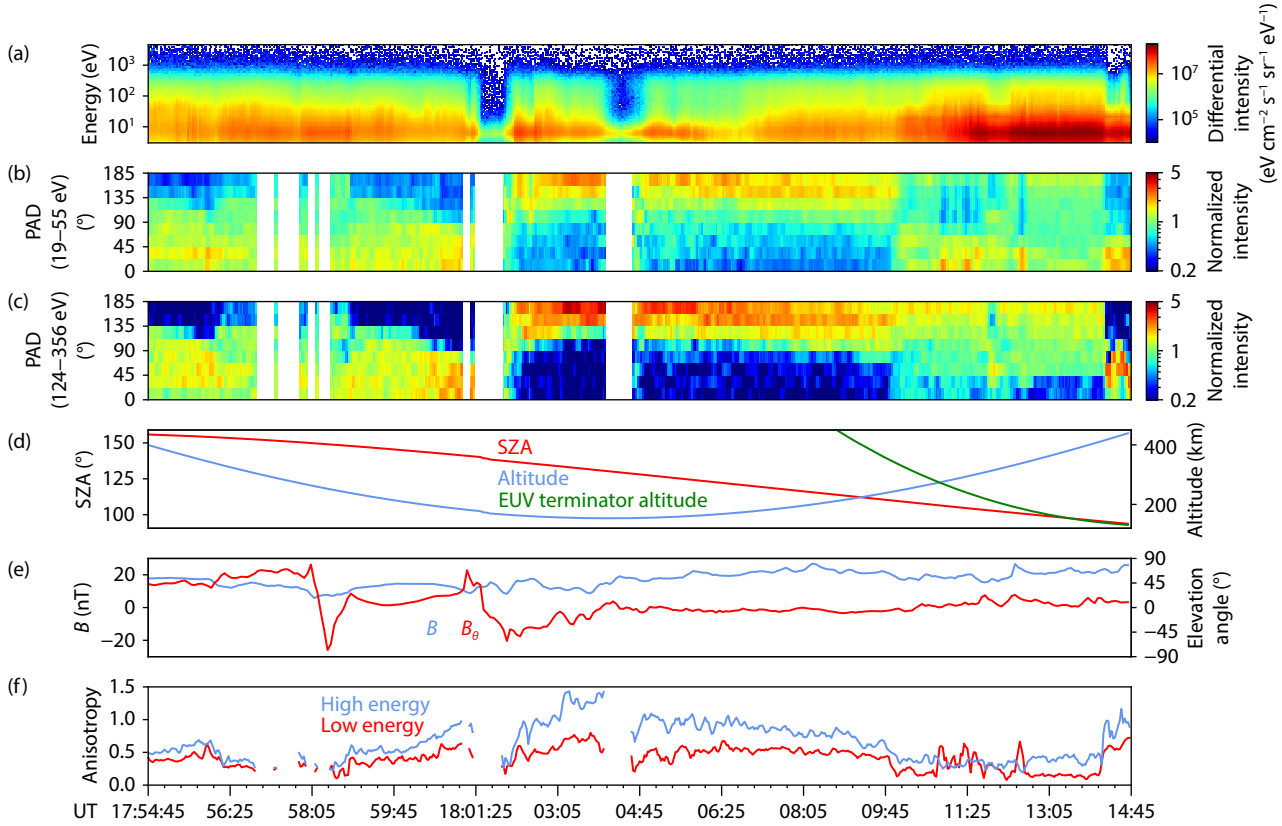

Figure 2. Similar to Figure 1 but for the SWEA suprathermal electron energy spectra measured during MAVEN orbit #475 on 27 December 2014. The green line in panel (d) represents the altitude at the EUV terminator adapted from Lillis et al. (2018).

features are compatible with the respective sources of different suprathermal electron populations. For instance, the low energy electrons on the dayside characterize photoelectrons produced isotropically in the Martian upper atmosphere and varying in response to the relatively stable solar EUV irradiance, whereas the low energy electrons on the nightside as well as the high energy electrons on both sides likely characterize SW electrons with PAD modulated by the ambient magnetic field orientation and varying in response to the highly variable upstream SW condition.

The calculation of the anisotropic factor from a SWEA spectrum is subject to several sources of uncertainty including counting statistics, finite angular resolution, and instrument sensitivity. A simple Monte Carlo approach is used to estimate the combined uncertainty. Specifically, we generate the mean SWEA energy spectrum at 160−200 km with SZA < 90° that characterizes locally produced dayside photoelectrons, with which we convert the omni-directional intensities at different energies to the counts recorded by the SWEA at each direction assuming a strictly isotropic PAD. Random counts are then added to these "ideal" counts according to Poissonian statistics, which are then converted back to the energy-dependent intensities at that direction taking into account the sensitivity variation among different angular bins. When integrated over the appropriate energy ranges, the above procedure allows independent anisotropic factors to be derived for both low and high energy electrons defined above. Based on a large number of random realizations, the mean anisotropic factor and the respective scattering could be obtained at any given suprathermal electron energy range. A similar procedure is also performed on the mean SWEA energy spectrum at 200−300 km with SZA > 150° that presumably characterizes SW electrons. We find that, for both choices of the suprathermal electron energy distribution, the uncertainty in the mean anisotropic factor is typically 0.14 with a scattering of 0.02. It is then reasonable to adopt an energy-independent threshold anisotropic factor of 0.2, corresponding to 3σ above the mean anisotropic factor from the Monte Carlo approach, as an upper limit to identify an observed PAD as isotropic.

3. Broad Characteristics of Suprathermal Electron Anisotropy

Our investigation of the variations of suprathermal electron PAD is based on the anisotropic factors for all SWEA spectra measured at altitudes below 700 km, corresponding to the location of the average photoelectron boundary on Mars (e.g. Garnier et al., 2017; Han QQ et al., 2019). To avoid sampling bias, we only consider the anisotropic factors determined for those spectra with valid intensity measurements covering all angular bins, and a total number of 1,269,252 individual measurements is thus selected for subsequent analyses.

We present in Figure 3 the occurrence rate of anisotropy for both low (upper panel) and high (lower panel) energy electrons to analyze the broad characteristics of suprathermal electron anisotropy. Xu SS et al. (2017a) designed a shape parameter (SP) to distinguish photoelectron energy spectra from SW electron spectra, based on the absolute difference in the derivative of suprathermal electron intensity with respect to energy between an observed SWEA spectrum and a template spectrum computed

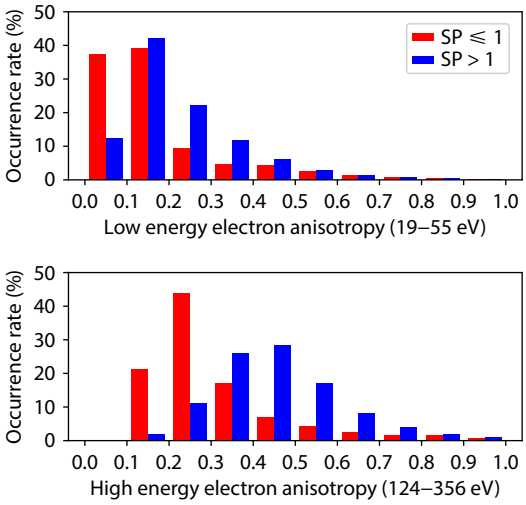

Figure 3. The occurrence rate of the anisotropic factor below 700 km in the Martian ionosphere, with the shape parameter (SP) of the spectra, identified by Xu SS et al. (2017a), indicated by red (SP≤ 1) and blue (SP > 1), respectively. The upper and lower panels compare the observations of low and high energy electrons.

from 60 visually confirmed SWEA photoelectron spectra. In general, a spectrum is identified as photoelectron spectrum if the SP of the spectrum is less than or equal to 1, otherwise, the spectrum is identified as SW spectrum. In Figure 3, the SP of the spectra is also indicated by red (SP ≤ 1) and blue (SP > 1).

The figure indicates that for photoelectrons with low energy (19−55 eV), 76% of the observed anisotropy is below 0.2, suggesting a near isotropic PAD (see Section 2). For SW electrons with low energy, the observed anisotropy occurs the most frequently between 0.1 and 0.2, with the total probability of observing isotropic PAD reaching 54%. The top panel indicates that the low energy electrons are more likely isotropic for both photoelectrons and SW electrons. Photoelectrons are isotropic due to the photoionization process as discussed in Section 2, while the high ratio of isotropic SW electrons suggests that isotropic photoelectron may also contribute to the measured low energy electron intensity, though the SP of which suggests a more SW electron like spectrum.

To be distinguished from the low energy electrons, the high energy electrons at 124−356 eV are nearly exclusively characterized by a strongly anisotropic PAD for both photoelectrons and SW electrons, with the probability of observing isotropic PAD decreasing to 21% and 2%, respectively. Photoelectrons with high energy are most likely observed at anisotropy between 0.2−0.3, with the probability of 44% and the probability of SW electron anisotropy is roughly Gaussian-like, centered at anisotropy between 0.5−0.6. The bottom panel suggests that SW electrons should be more anisotropic than photoelectrons and the increase of photoelectron anisotropy may caused by the increasing portion of SW electrons at high energy range.

The above discussion indicates that different categories of suprathermal electron should be considered simultaneously in order to interpret properly the PAD observations. In practice, each anisotropy distribution displayed in Figure 3 reflects the observa-

tion of either one particular category of suprathermal electron or the combination of more than one category. The case studies in Figures 1 and 2 also suggest that the PADs of electrons with different energies are independent with whether the photoelectron peak is visible or not. In addition to distinguishing different categories of suprathermal electron via spectra shape, the variations of the anisotropy should be able to provide more insights into the contribution of each category of suprathermal electron, which we present in the following section.

4. Variations of Suprathermal Electron Anisotropy

We start with the altitudinal variation of the suprathermal electron anisotropy in Figure 4, with the dayside and nightside situations indicated by red and blue, respectively. The error bars encompass the range from 25% to 75% quartiles. The figure reveals clearly that on the dayside, the low energy electrons become progressively more anisotropic with increasing altitude, from isotropic at the bottom to slightly anisotropic at the top, whereas for high energy electrons, a roughly constant anisotropic factor of ~0.4 is observed at all altitudes. In contrast, the nightside anisotropy tends to decrease with increasing altitude for both low and high energy electrons, from 0.38 at the bottom to 0.28 at the top when the electron energy is 19−55 eV and more rapidly from 0.68 to 0.37 over the same altitude range when the electron energy is 124−356 eV. The above trends could also be seen in Figure 5 where we display the full altitude and SZA variations of suprathermal electron anisotropy, over the altitude range of 140−700 km with a binsize of 20 km and over the SZA range of 20°−140° with a binsize of 10°. Dayside regions with SZA < 20° and nightside regions with SZA > 140° are relatively poorly sampled, which does not allow statistically robust variations to be achieved. Note that different color scales are used for displaying the low and high energy electrons due to their different degrees of anisotropy.

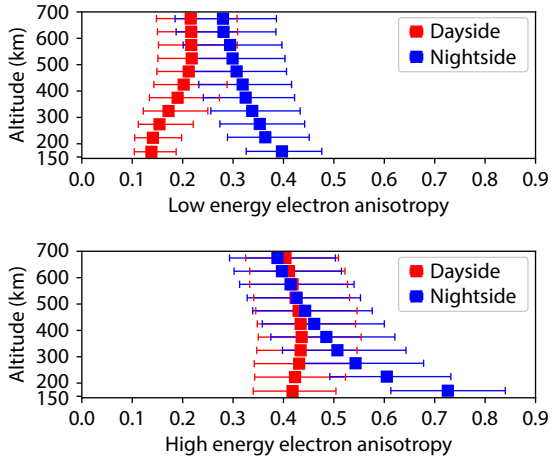

Figure 4. The altitudinal variation of the anisotropic factor, distinguishing between the low and high energy electrons, and also between the dayside and nightside. The error bars encompass the range from 25% to 75% quartiles.

We speculate that the bulk of the dayside low energy electrons characterize photoelectrons, either produced locally via photoionization or transported from the low altitude source regions. In general, the magnetic field intensity in the Martian ionosphere tends to increase with decreasing altitude, as implied by an upward magnetic pressure gradient force exerted on both the dayside and nightside ions (e.g. Wu XS et al., 2019b). This means that the upward transport of photoelectrons is accompanied by the conversion of perpendicular momentum to parallel momentum as required by the conservation of the first adiabatic invariant. Such a process is likely responsible for the observation of a more anisotropic PAD at high altitudes. This is exactly the trends seen in Figures 4 and 5, confirming our speculation. Despite this, we cannot rule out the possibility that regions at higher altitudes

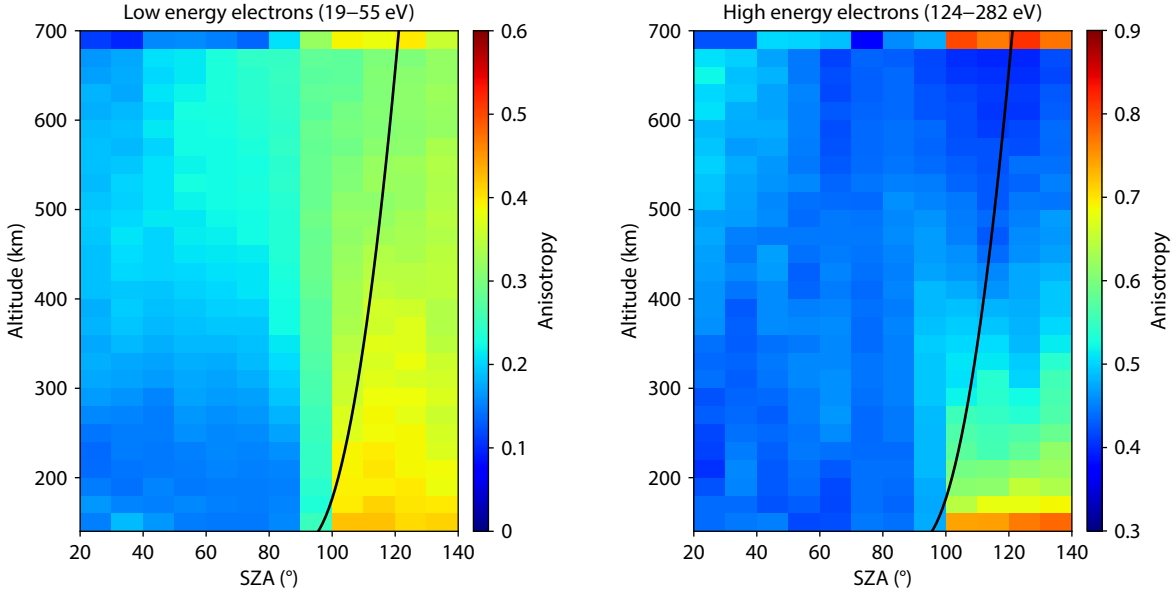

Figure 5. The anisotropy distribution for both low and high energy electrons over the altitude range of 140−700 km with a binsize of 20 km and over the SZA range of 20°−140° with a binsize of 10°. Regions with less than 10 individual measurements are deemed as statistically poor and color-coded by white. The black line in each panel shows the EUV terminator of Lillis et al. (2018).

feel a larger contribution from precipitating SW electrons with an anisotropic PAD.

On the nightside, the observed altitude variation of the anisotropy, showing a common behavior for both low and high energy electrons, could be interpreted by assuming that they mainly characterize SW electrons. In addition, the SW electrons would collide with atmospheric CO_2 and O, producing secondary electrons isotropically. Since the impact ionization rate increases with decreasing altitude in response to the enhanced neutral densities, we expect that the secondary electrons, which are isotropic, should be more easily observed at relatively low altitudes. This is in disagreement with the trends seen in Figures 4 and 5, indicating that the contribution of secondary electron production, if present, is likely of minor importance.

Similar to the dayside photoelectron transport, the altitudinal variation of the suprathermal electron anisotropy during nightside SW precipitation is also strongly affected by the ambient magnetic field configuration. In particular, the field-aligned momentum of any SW electron is converted to perpendicular momentum with decreasing altitude, which means that the electron PAD over the downward hemisphere continuously varies along the route of precipitation. The precipitating electron could eventually be bounced backwards at low altitudes and form the upward hemisphere of the electron PAD. In the ideal situation of no electron loss via collisions with atmospheric neutrals, the electron PAD is always near isotropic, with identical contributions from the upward and downward hemispheres. In reality, a portion of the field-aligned electrons can penetrate down to deep regions of the Martian atmosphere where they make frequent collisions with ambient neutrals to form the so-called loss cone in PAD. Such a process effectively increases the electron anisotropy with decreasing altitude, as suggested by the nightside SWEA observations.

Since the change in electron PAD during precipitation is expected to be controlled by the ambient magnetic field configuration, we further compare in Figure 6 the altitude variations of the anisotropy between the northern and southern hemispheres. The figure suggests that precipitating SW electrons tend to be less anisotropic over the southern hemisphere of Mars where strong crustal magnetic anomalies are preferentially located (e.g. Acuna et al., 1998; Connerney et al., 1999). Because the size of the SW electron loss cone is proportional to the ratio of the minimum magnetic field strength to the maximum magnetic field strength along the route of precipitation, the strongly magnetized regions are naturally characterized by a narrower loss cone and consequently a more isotropic PAD as compared to the weakly magnetized regions. However, we caution that the loss cone interpretation does not distinguish between SW electrons precipitating along open magnetic fields lines or photoelectrons transported over large horizontal scales along closed magnetic field lines with one footprint on the dayside and the other footprint on the nightside. However, the occurrence rate of the latter magnetic field configuration is much lower than the former according to Xu SS et al. (2017a), implying that, as a first order approximation, the contribution from cross-terminator photoelectron transport to the PAD of nightside electrons could be ignored.

The situation for the dayside high energy electrons is more complicated in that the PAD is always anisotropic, which must be indicative of a SW origin. However, SW electron precipitation cannot explain the apparent constancy of the observed anisotropy with altitude, because otherwise the altitude variation should closely resemble the nightside trend as a result of collisions with atmospheric neutrals within the loss cone. We speculate that the observation for dayside high energy electrons is indicative of the combined outcome of SW electrons and locally produced photoelectrons, of which the latter tend to drive the electron PAD towards more isotropic. Obviously, the contribution from photoelectrons should be more pronounced at low altitudes in order to maintain a near constant degree of anisotropy. Our conjecture is also supported by Figure 6 where we observe a visible trend of slightly more anisotropic high energy electrons in the weakly

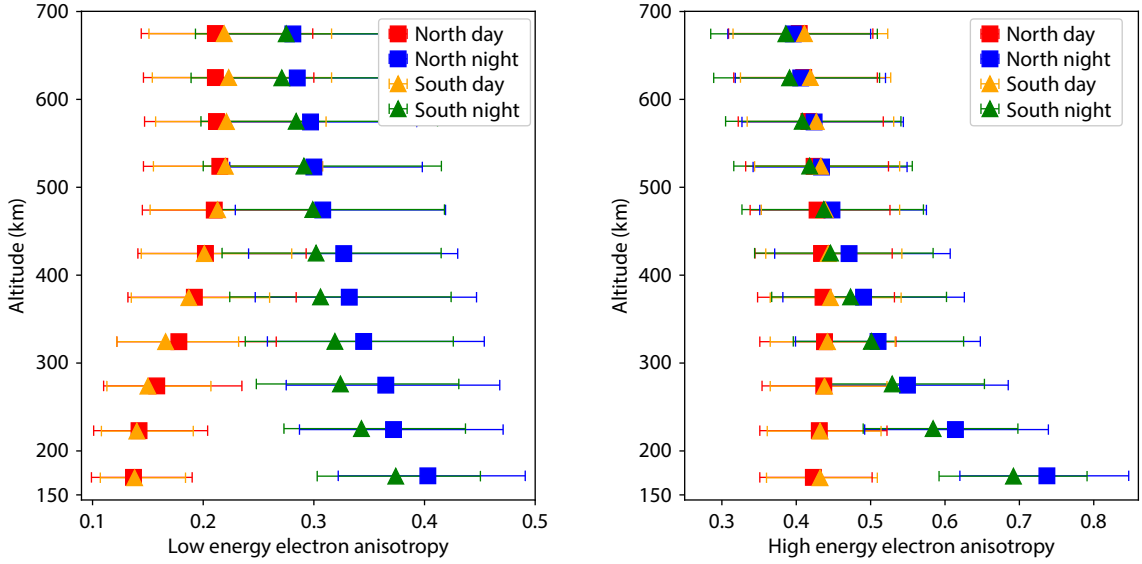

Figure 6. Similar to Figure 4 but distinguishing between the northern and southern hemispheres of Mars. The observations of low and high energy electrons are presented in the left and right panels, respectively.

magnetized regions relative to the strongly magnetized regions as explained above. This makes a good case for which the interpretation of the SWEA observations relies on the combination of two suprathermal electron populations.

To better illustrate the role of the ambient magnetic field configuration, we present the geographic distribution of suprathermal electron anisotropy over three altitude ranges indicated in the figure legend, left for the dayside and right for the nightside, respectively. The situations for the low and high energy electrons are presented in Figures 7 and 8, using different color scales. The crustal magnetic field model of Morschhauser et al. (2014) is superimposed in each panel for a fixed altitude of 400 km. The scenario described above is further supported by the features seen in these figures. For instance, the SWEA observations reveal an increase in anisotropy towards lower altitudes, as well as a decrease in anisotropy towards regions with stronger magnetic fields, for both low and high energy electrons on the nightside. Meanwhile, these figures also reveal a weak tendency of enhanced anisotropy at high altitudes over strong crustal magnetic anomalies for dayside low energy electrons, as well as a reduced anisotropy at low altitudes over the same regions for dayside high energy electrons. As explained above, the former is likely linked to the upward photoelectron transport which tends to be more efficient near strong crustal anomalies characterized by preferred vertical field lines (e.g. Cui J et al., 2018), and the latter could be interpreted by the enhanced contribution from precipitating SW electrons.

Finally, we note that photoelectron production in the Martian ionosphere critically depends on the solar EUV irradiance (e.g. Peterson et al., 2016; Wu XS et al., 2020a), whereas the pattern of SW electron precipitation is controlled by the upstream SW condition (e.g. Lillis and Brain, 2013; Lillis et al., 2018; Niu DD et al., 2020). These findings imply that the observed characteristics of suprathermal electron PAD or anisotropy also depend on these two controlling factors. In Figures 9 and 10, we compare the occurrence rates of suprathermal electron PAD either between low and high solar activity conditions, or between low and high upstream SW conditions. The low and high solar activity conditions are defined with the solar radio index at 10.7 cm referred to the Earth below and above 100 solar flux unit (SFU, 10^{-22} W m^{-2} Hz^{-1}), whereas the low and high upstream SW conditions are defined with the SW dynamic pressure below and above 0.65 nPa, respectively, where the SW dynamic pressure from each individual MAVEN orbit is adapted from Niu DD et al. (2020) based on the MAVEN Solar Wind Ion Analyzer measurements (Halekas et al., 2015).

In general, Figures 9 and 10 do not reveal any substantial difference between the various conditions under investigation. However, some interesting features are tentatively visible such as the observation of a slightly more isotropic PAD for dayside high energy electrons under high solar activities as compared to low solar activities, which is consistent with the expected trend since the contribution from photoelectrons (relative to SW electrons) increases with increasing solar EUV irradiance. A similar trend is not seen for dayside low energy electrons, essentially demonstrating a common anisotropy distribution irrespective of solar activity, which is also expected due to the predominance of photoelectrons at the relevant energies. The accumulation of more SWEA data

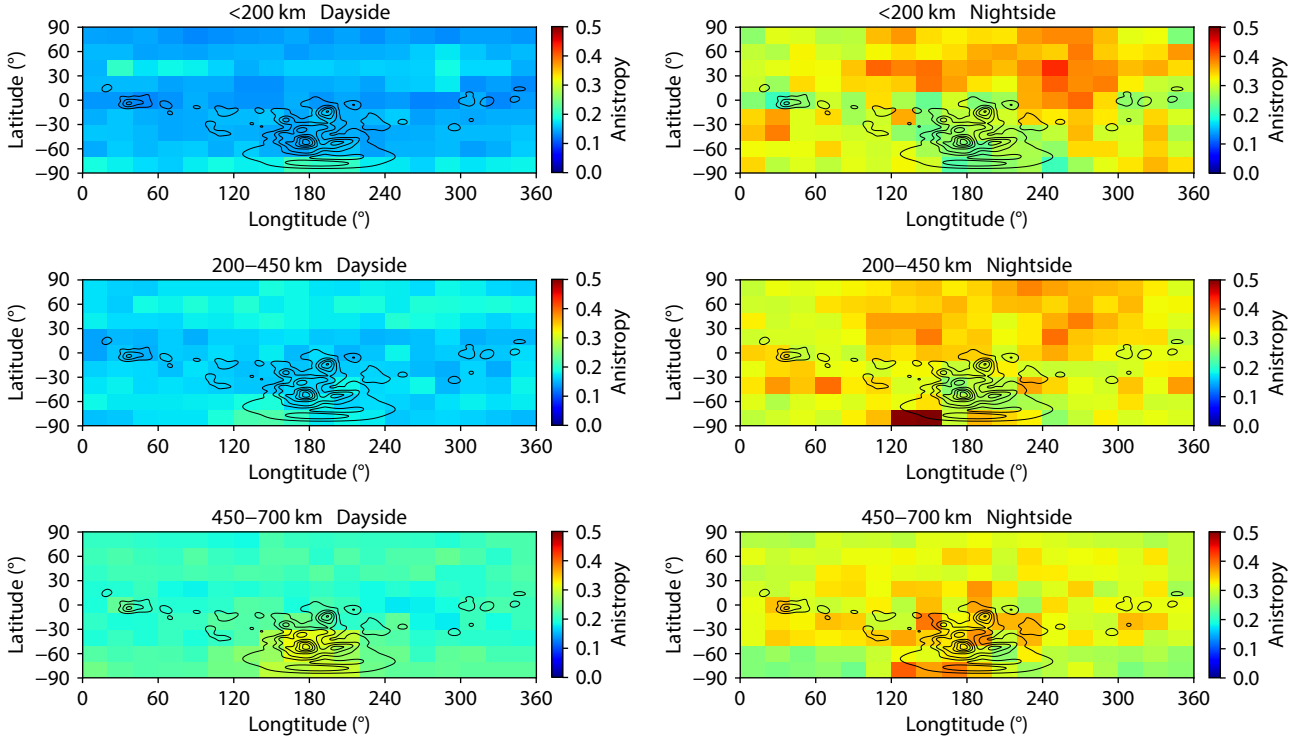

Figure 7. The geographic distribution of the low energy electron anisotropy over three altitude ranges, 140–200 km (top), 200–450 km (middle), and 450–700 km (bottom). The dayside and nightside situations are indicated separately in the left and right panels. The crustal magnetic field model of Morschhauser et al. (2014) is superimposed in each panel for a fixed altitude of 400 km.

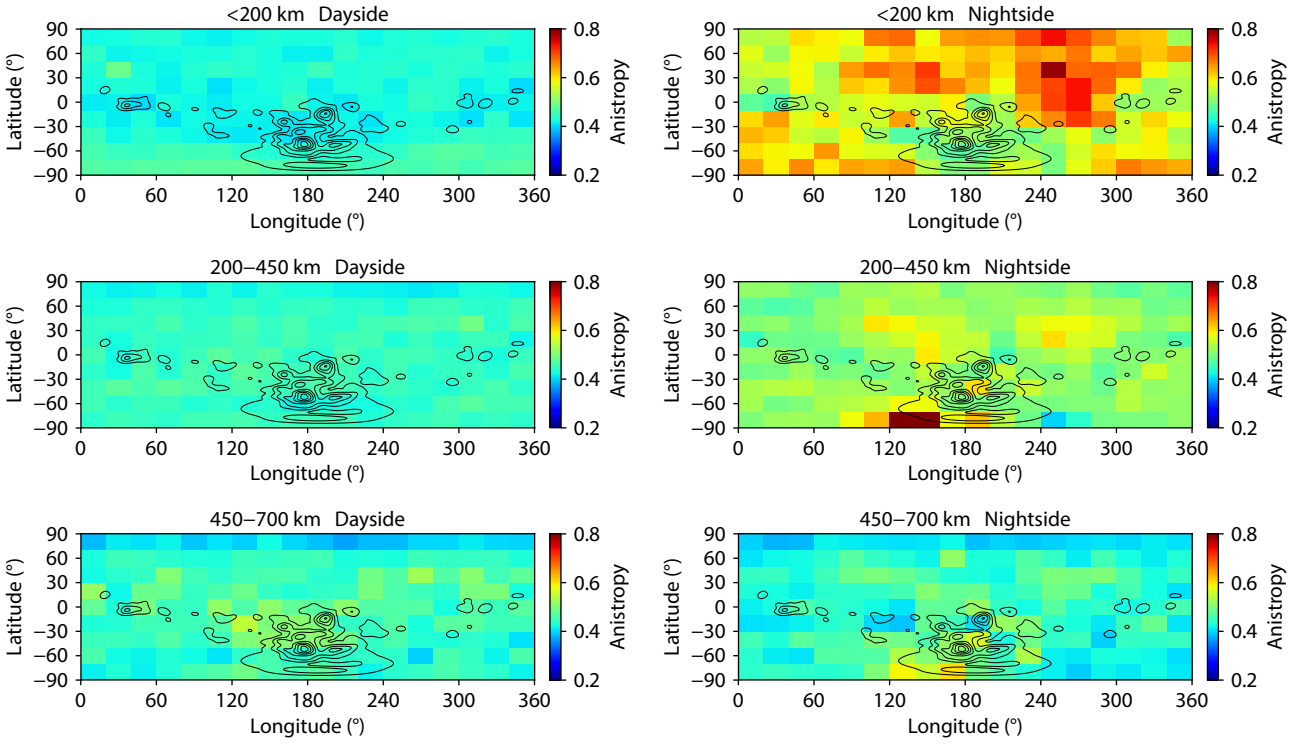

Figure 8. Similar to Figure 7 but for the geographic distribution of the high energy electron anisotropy.

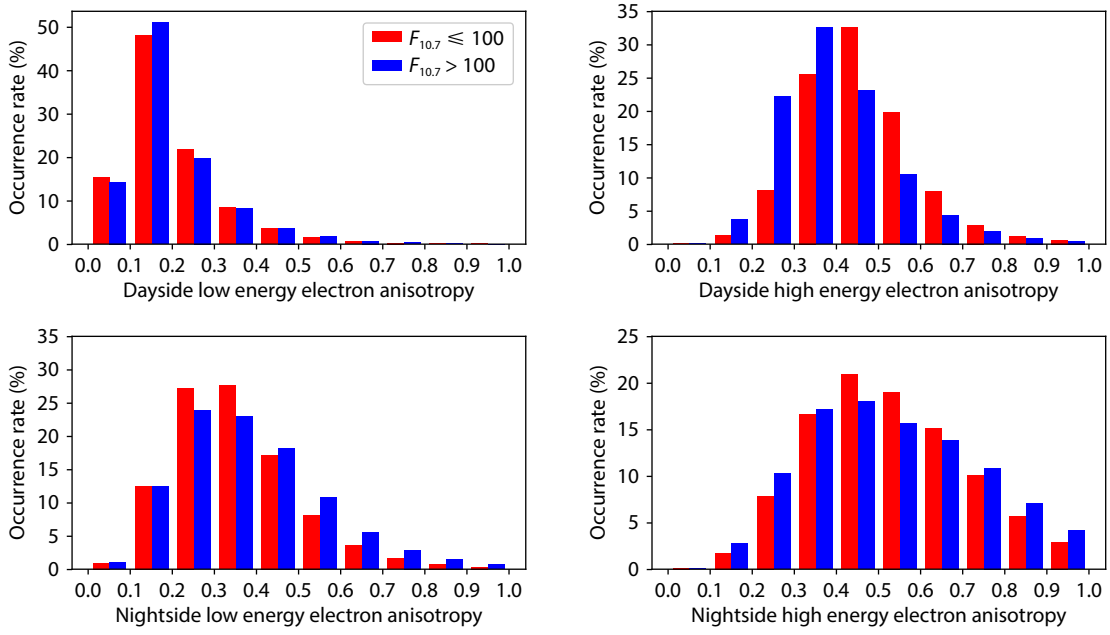

Figure 9. The occurrence rate of the anisotropic factor below 700 km in the Martian ionosphere, distinguishing between low (red) and high (blue) solar activity conditions. The respective solar radio indexes at 10.7 cm are below and above 100 SFU, both referred to the Earth.

covering a broader range of spaceweather conditions at Mars (Lee et al., 2017) should help elucidate the variations of suprathermal electron PAD with both solar activity and upstream SW conditions.

5. Discussion: The Diversity of Suprathermal Electron PAD

In addition to the anisotropic factor discussed so far, the full PAD measured by the SWEA contains more information on the origin and transport of suprathermal electrons along magnetic field lines within the Martian ionosphere (e.g. Weber et al., 2017). For demonstrative purposes, we present in Figure 11 several categories of SWEA-based PAD for low energy electrons at 19–55 eV, which, according to Section 4, characterize either photoelectrons or precipitating SW electrons. The corresponding geophysical parameters, as well as the anisotropic factors, are tabulated in the

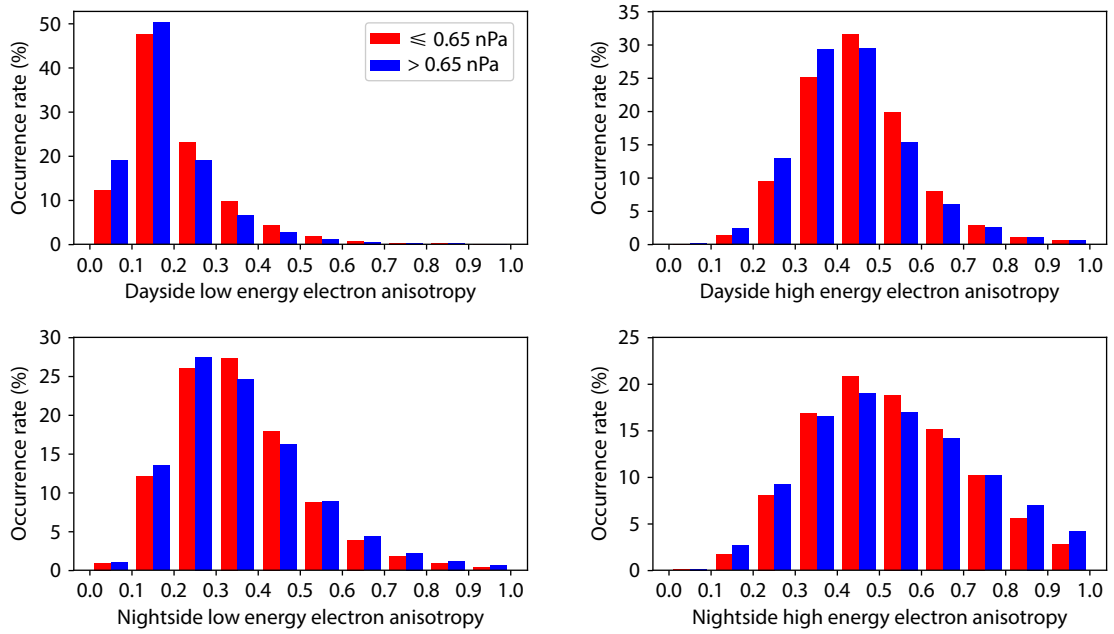

Figure 10. Similar to Figure 9 but distinguishing between low (red) and high (blue) upstream SW conditions. The respective SW dynamic pressures are below and above 0.65 nPa.

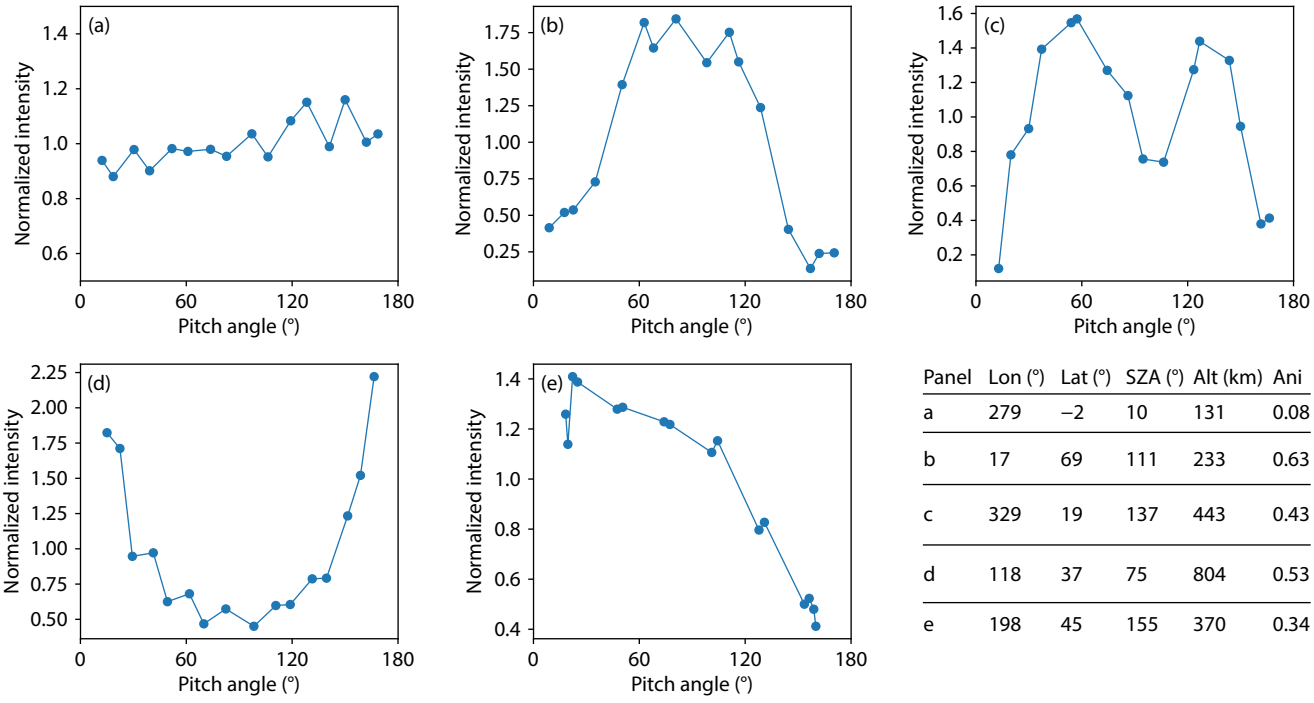

Panel	Lon (°)	Lat (°)	SZA (°)	Alt (km)	Ani
a	279	−2	10	131	0.08
b	17	69	111	233	0.63
c	329	19	137	443	0.43
d	118	37	75	804	0.53
e	198	45	155	370	0.34

Figure 11. Typical types of the measured PAD shape for low energy electrons. In order: (a) isotropic, (b) two-sided loss cone, (c) conical, (d) field-aligned, and (e) one-sided loss cone. The corresponding geophysical parameters, including the altitude, SZA, longitude, and latitude, along with the computed anisotropic factor, are tabulated for reference.

figure for reference.

In panel (a), we present an apparently isotropic PAD with an anisotropy as small as ≈0.08, measured at 131 km under the near subsolar condition. Such a PAD is clearly caused by the solar EUV ionization of atmospheric neutrals. The remaining panels show a variety of PAD shapes, all anisotropic and modulated by suprathermal electron transport along magnetic field lines with different configurations. Under these circumstances, the conversion between the parallel and perpendicular components of the suprathermal electron velocity, as well as the absorption of suprathermal electrons by the atmosphere via collisions at low altitudes, are two crucial factors controlling the variation of the observed anisotropy.

In panel (b), we present a typical PAD with two-sided loss cone

measured at 233 km on the nightside of Mars. This PAD is frequently observed in regions with a closed magnetic field configuration with both footprints in the darkness, where the electrons are trapped within the magnetic flux tube and those electrons within the loss cone are able to reach the low altitude regions and be lost due to atmospheric absorption. The conical PAD as the one shown in panel (c), measured on the nightside at 443 km, has been proposed to be formed during photoelectron transport along cross-terminator magnetic field lines (Cao YT et al., 2020). As modeled by Cao YT et al. (2021), the reduction in the center of the measured PAD is related to the conversion from perpendicular to parallel momentum, whereas the reduction at the two ends is caused by atmospheric absorption within the loss cone. In addition, Ulusen et al. (2011) suggested that precipitating SW electrons could also form a similar PAD through the merging of neighboring open field lines.

Panel (d) presents a typical field-aligned PAD measured at 804 km on the dayside. Such a PADs shape is likely the outcome of photoelectron transport along closed magnetic field lines with both footprints on the dayside. This is also due to the conversion between the perpendicular and parallel components of the photoelectron velocity in a varying magnetic field. We also note that panel (d) is to be distinguished from panel (b) which characterize closed field lines with both footprints on the nightside, due to the replenishment of photoelectrons persistently produced via solar ionization at low altitudes. In panel (e), we show a PAD with one-sided loss cone covering a broad pitch angle range of 120°−180°, measured at 370 km in the deep nightside. As discussed in Section 4, such a PAD is formed during SW electron precipitation when the suprathermal electrons within the loss cone are absorbed by the atmosphere at low altitudes.

6. Conclusions

Suprathermal electrons are an important population of the Martian ionosphere, which could be either produced by solar EUV and X-ray ionization on the dayside or supplied from the SW on both the dayside and nightside. Suprathermal electrons from different sources clearly present different characteristics of PAD. This study is dedicated to an in-depth investigation of the suprathermal electron PAD, by virtue of the exceptionally large data set accumulated by the MAVEN SWEA instrument (Mitchell et al., 2016).

Though the available SWEA measurements reveal a variety of suprathermal electron PADs in the Martian ionosphere (e.g. Weber et al., 2017), all PADs modulated by suprathermal electron transport tend to be anisotropic and well described by a common parameter irrespective of the detailed shape. Throughout the study, we focus on such a parameter, termed as the anisotropy and defined as the standard deviation of suprathermal electron intensity among different directions which is then normalized by the mean omni-directional intensity. To be distinguished from some previous studies (e.g. Weber et al., 2017; Xu SS et al., 2019), the measured PADs at two representative energy ranges are considered, including the low energy range at 19−55 eV and the high energy range at 124−356 eV, in order to distinguish between suprathermal electrons of different origins.

The available SWEA measurements reveal several interesting characteristics of the suprathermal electron anisotropy, which could be summarized as follows: (1) Low energy electrons are in general more isotropic than high energy electrons; (2) Dayside electrons are in general more isotropic than nightside electrons; (3) On the dayside, the anisotropy increases with increasing altitude at low energies but remains roughly constant at high energies, whereas on the nightside, the anisotropy decreases with increasing altitude at all energies; (4) Electrons tend to be more isotropic in strongly magnetized regions than in weakly magnetized regions, especially on the nightside; (5) No unambiguous variation in anisotropy with either solar activity or upstream SW condition can be identified.

The observations described above are supposed to be caused by a mixture of several independent processes, whose relative contributions to the observed suprathermal electron anisotropy vary with the electron energy, altitude, SZA, and magnetic field configuration. The conversion between the parallel and perpendicular components of the suprathermal electron velocity, as well as the absorption of suprathermal electrons by the atmosphere via collisions at low altitudes, are two crucial factors controlling the variation of the observed anisotropy. On the one hand, photoelectrons are born isotropic, but at high altitudes where photoelectron transport becomes important, they are driven towards a more anisotropic state in response to the conversion from perpendicular to parallel momentum with increasing altitude. Such a process is more prominent in the strongly magnetized regions where the field lines are preferentially vertical and facilitate upward transport. On the other hand, SW electrons become more anisotropic as they precipitate downwards along open magnetic field lines in the direction of increasing magnetic field intensity, primarily due to the absorption of near field-aligned electrons within the loss cone by the atmosphere. Such a process should instead be more prominent in the weakly magnetized regions where the loss cone tends to be broader. In general, the suprathermal electron is more isotropic if the local produced photoelectron is the dominant source and the anisotropy of the suprathermal electron increases with increasing portion of the transported photoelectron and SW electron. The above characteristics emphasize that the PADs of suprathermal electrons with different energies should be analyzed respectively.

Despite that the proposed scenarios are able to successfully interpret most observations in a qualitative manner, a more detailed and quantitative comparison is impossible at the level of analysis presented here. For instance, a full interpretation of the altitudinal variation of suprathermal electron anisotropy on the nightside of Mars requires realistic magnetic field configurations to be imposed, realistic PADs of SW electrons at the top to be adopted, and realistic interactions of precipitating SW electrons with ambient neutrals to be monitored. Such a detailed modeling is left for follow-up investigations.

Open Research

The MEx dataset used in this work is publicly available at the Planetary Plasma Interactions Node of the Nasa Planetary Data System public archives (https://pds-ppi.igpp.ucla.edu/index.jsp).

Acknowledgments

The authors acknowledge supports from the National Natural Science Foundation of China through grants 42241114, 42274218 and 42304166. This work is also supported by the B-type Strategic Priority Program No. XDB41000000 funded by the Chinese Academy of Sciences, the pre-research project on Civil Aerospace Technologies No. D020105 funded by China's National Space Administration, the Guangdong Basic and Applied Research Foundation Project 2021A1515110271, and the Key Laboratory of Geospace Environment, Chinese Academy of Sciences, University of Science & Technology of China.

References

Acuna, M. H., Connerney, J. E. P., Wasilewski, P., Lin, R. P., Anderson, K. A., Carlson, C. W., Mcfadden, J., Curtis, D. W., Mitchell, D., … Ness, N. F. (1998). Magnetic field and plasma observations at mars: initial results of the mars global surveyor mission. *Science*, *279*(5357), 1676–1680. https://doi.org/10.1126/science.279.5357.1676

Adams, D., Xu, S., Mitchell, D. L., Lillis, R. J., Fillingim, M., Andersson, L., Fowler, C., Connerney, J. E. P., Espley, J., and Mazelle, C. (2018). Using magnetic topology to probe the sources of Mars' nightside ionosphere. *Geophys. Res. Lett.*, *45*(22), 12190–12197. https://doi.org/10.1029/2018GL080629

Cao, Y. T., Cui, J., Ni, B. B., Wu, X. S., Luo, Q., and He, Z. G. (2020). Bidirectional electron conic observations for photoelectrons in the Martian ionosphere. *Earth Planet. Phys.*, *4*(4), 403–407. https://doi.org/10.26464/epp2020037

Cao, Y. T., Cui, J., Wu, X. S., Niu, D. D., Lai, H. R., Ni, B. B., Luo, Q., Yu, J., and Wei, Y. (2021). A survey of photoelectrons on the nightside of mars. *Geophys. Res. Lett.*, *48*(2), e89998. https://doi.org/10.1029/2020GL089998

Coates, A. J., Tsang, S. M. E., Wellbrock, A., Frahm, R. A., Winningham, J. D., Barabash, S., Lundin, R., Young, D. T., and Crary, F. J. (2011). Ionospheric photoelectrons: comparing Venus, earth, mars and Titan. *Planet. Space Sci.*, *59*(10), 1019–1027. https://doi.org/10.1016/j.pss.2010.07.016

Connerney, J. E. P., Acuna, M. H., Wasilewski, P. J., Ness, N. F., Reme, H., Mazelle, C., Vignes, D., Lin, R. P., Mitchell, D. L., and Cloutier, P. A. (1999). Magnetic lineations in the ancient crust of mars. *Science*, *284*(5415), 794–798. https://doi.org/10.1126/science.284.5415.794

Connerney, J. E. P., Espley, J., Lawton, P., Murphy, S., Odom, J., Oliversen, R., and Sheppard, D. (2015). The MAVEN magnetic field investigation. *Space Sci. Rev.*, *195*(1-4), 257–291. https://doi.org/10.1007/s11214-015-0169-4

Cui, J., Wu, X. S., Xu, S. S., Wang, X. D., Wellbrock, A., Nordheim, T. A., Cao, Y. T., Wang, W. R., Sun, W. Q., … Wei, Y. (2018). Ionization efficiency in the dayside Martian upper atmosphere. *Astrophys. J. Lett.*, *857*(2), L18. https://doi.org/10.3847/2041-8213/aabcc6

Cui, J., Cao, Y. T., Wu, X. S., Xu, S. S., Yelle, R. V., Stone, S., Vigren, E., Edberg, N. J. T., Shen, C. L., … Wei, Y. (2019). Evaluating local ionization balance in the nightside Martian upper atmosphere during *MAVEN* deep dip campaigns. *Astrophys. J. Lett.*, *876*(1), L12. https://doi.org/10.3847/2041-8213/ab1b34

Fowler, C. M., Andersson, L., Ergun, R. E., Morooka, M., Delory, G., Andrews, D. J., Lillis, R. J., Mcenulty, T., Weber, T. D., … Jakosky, B. M. (2015). The first in situ electron temperature and density measurements of the Martian nightside ionosphere. *Geophys. Res. Lett.*, *42*(21), 8854–8861. https://doi.org/10.1002/2015GL065267

Fox, J. L., Galand, M. I., and Johnson, R. E. (2008). Energy deposition in planetary atmospheres by charged particles and solar photons. *Space Sci. Rev.*, *139*(1-4), 3–62. https://doi.org/10.1007/s11214-008-9403-7

Frahm, R. A., Sharber, J. R., Winningham, J. D., Wurz, P., Liemohn, M. W., Kallio, E., Yamauchi, M., Lundin, R., Barabash, S., … McKenna-Lawler, S. (2006a). Locations of atmospheric photoelectron energy peaks within the mars environment. *Space Sci. Rev.*, *126*(1), 389–402. https://doi.org/10.1007/s11214-006-9119-5

Frahm, R. A., Winningham, J. D., Sharber, J. R., Scherrer, J. R., Jeffers, S. J., Coates, A. J., Linder, D. R., Kataria, D. O., Lundin, R., … Dierker, C. (2006b). Carbon dioxide photoelectron energy peaks at Mars. *Icarus*, *182*(2), 371–382. https://doi.org/10.1016/j.icarus.2006.01.014

Garnier, P., Steckiewicz, M., Mazelle, C., Xu, S., Mitchell, D., Holmberg, M. K. G., Halekas, J. S., Andersson, L., Brain, D. A., … Jakosky, B. M. (2017). The Martian photoelectron boundary as seen by MAVEN. *J. Geophys. Res.: Space Phys.*, *122*(10), 10472–10485. https://doi.org/10.1002/2017JA024497

Girazian, Z., Mahaffy, P., Lillis, R. J., Benna, M., Elrod, M., Fowler, C. M., and Mitchell, D. L. (2017). Ion densities in the Nightside ionosphere of mars: Effects of electron impact ionization. *Geophys. Res. Lett.*, *44*(22), 11248–11256. https://doi.org/10.1002/2017GL075431

Halekas, J. S., Taylor, E. R., Dalton, G., Johnson, G., Curtis, D. W., McFadden, J. P., Mitchell, D. L., Lin, R. P., and Jakosky, B. M. (2015). The solar wind ion analyzer for MAVEN. *Space Sci. Rev.*, *195*(1-4), 125–151. https://doi.org/10.1007/s11214-013-0029-z

Han, Q. Q., Fan, K., Cui, J., Wei, Y., Fraenz, M., Dubinin, E., Chai, L. H., Rong, Z. J., Wan, W. X., … Connerney, J. E. P. (2019). The relationship between photoelectron boundary and steep electron density gradient on mars: MAVEN observations. *J. Geophys. Res.: Space Phys.*, *124*(10), 8015–8022. https://doi.org/10.1029/2019JA026739

Lee, C. O., Hara, T., Halekas, J. S., Thiemann, E., Chamberlin, P., Eparvier, F., Lillis, R. J., Larson, D. E., Dunn, P. A., … Jakosky, B. M. (2017). MAVEN observations of the solar cycle 24 space weather conditions at Mars. *J. Geophys. Res.: Space Phys.*, *122*(3), 2768–2794. https://doi.org/10.1002/2016JA023495

Liemohn, M. W., Frahm, R. A., Winningham, J. D., Ma, Y., Barabash, S., Lundin, R., Kozyra, J. U., Nagy, A. F., Bougher, S. M., … Dierker, C. (2006). Numerical interpretation of high-altitude photoelectron observations. *Icarus*, *182*(2), 383–395. https://doi.org/10.1016/j.icarus.2005.10.036

Lillis, R. J., and Brain, D. A. (2013). Nightside electron precipitation at Mars: Geographic variability and dependence on solar wind conditions. *J. Geophys. Res.: Space Phys.*, *118*(6), 3546–3556. https://doi.org/10.1002/jgra.50171

Lillis, R. J., Mitchell, D. L., Steckiewicz, M., Brain, D., Xu, S. S., Weber, T., Halekas, J., Connerney, J., Espley, J., … Eparvier, F. (2018). Ionizing electrons on the Martian nightside: structure and variability. *J. Geophys. Res.: Space Phys.*, *123*(5), 4349–4363. https://doi.org/10.1029/2017JA025151

Mantas, G. P., and Hanson, W. B. (1979). Photoelectron fluxes in the Martian ionosphere. *J. Geophys. Res.: Space Phys.*, *84*(A2), 369–385. https://doi.org/10.1029/JA084iA02p00369

Mitchell, D. L., Mazelle, C., Sauvaud, J. A., Thocaven, J. J., Rouzaud, J., Fedorov, A., Rouger, P., Toublanc, D., Taylor, E., … Jakosky, B. M. (2016). The MAVEN solar wind electron analyzer. *Space Sci. Rev.*, *200*(1-4), 495–528. https://doi.org/10.1007/s11214-015-0232-1

Morschhauser, A., Lesur, V., and Grott, M. (2014). A spherical harmonic model of the lithospheric magnetic field of mars. *J. Geophys. Res.: Planets*, *119*(6), 1162–1188. https://doi.org/10.1002/2013JE004555

Nagy, A. F., Winterhalter, D., Sauer, K., Cravens, T. E., Brecht, S., Mazelle, C., Crider, D., Kallio, E., Zakharov, A., … Trotignon, J. G. (2004). The plasma environment of mars. *Space Sci. Rev.*, *111*(1-2), 33–114. https://doi.org/10.1023/B:SPAC.0000032718.47512.92

Niu, D. D., Cui, J., Gu, H., Wu, X. S., Wu, S. Q., Lu, H. Y., Chai, L. H., and Wei, Y. (2020). Energetic electron depletions in the Nightside Martian upper atmosphere revisited. *J. Geophys. Res.: Space Phys.*, *125*(4), e2019JA027670. https://doi.org/10.1029/2019JA027670

Peterson, W. K., Thiemann, E. M. B., Eparvier, F. G., Andersson, L., Fowler, C. M., Larson, D., Mitchell, D., Mazelle, C., Fontenla, J., … Jakosky, B. (2016). Photoelectrons and solar ionizing radiation at Mars: Predictions versus MAVEN observations. *J. Geophys. Res.: Space Phys.*, *121*(9), 8859–8870. https://doi.org/10.1002/2016JA022677

Safaeinili, A., Kofman, W., Mouginot, J., Gim, Y., Herique, A., Ivanov, A. B., Plaut, J. J., and Picardi, G. (2007). Estimation of the total electron content of the Martian ionosphere using radar sounder surface echoes. *Geophys. Res. Lett.*, *34*(23), L23204. https://doi.org/10.1029/2007GL032154

Sakai, S., Rahmati, A., Mitchell, D. L., Cravens, T. E., Bougher, S. W., Mazelle, C., Peterson, W. K., Eparvier, F. G., Fontenla, J. M., and Jakosky, B. M. (2015). Model insights into energetic photoelectrons measured at Mars by MAVEN. *Geophys. Res. Lett.*, *42*(21), 8894–8900. https://doi.org/10.1002/

2015GL065169

Shane, A., Liemohn, M., Florie, C., and Xu, S. S. (2019). Misbehaving high-energy electrons: evidence in support of ubiquitous wave-particle interactions on dayside Martian closed crustal magnetic fields. *Geophys. Res. Lett.*, *46*(21), 11689–11697. https://doi.org/10.1029/2019GL084919

Steckiewicz, M., Mazelle, C., Garnier, P., André, N., Penou, E., Beth, A., Sauvaud, J. A., Toublanc, D., Mitchell, D. L., … Jakosky, B. M. (2015). Altitude dependence of nightside Martian suprathermal electron depletions as revealed by MAVEN observations. *Geophys. Res. Lett.*, *42*(21), 8877–8884. https://doi.org/10.1002/2015GL065257

Steckiewicz, M., Garnier, P., André, N., Mitchell, D. L., Andersson, L., Penou, E., Beth, A., Fedorov, A., Sauvaud, J. A., … Jakosky, B. M. (2017). Comparative study of the Martian suprathermal electron depletions based on Mars Global Surveyor, Mars Express, and Mars Atmosphere and Volatile EvolutioN mission observations. *J. Geophys. Res.: Space Phys.*, *122*(1), 857–873. https://doi.org/10.1002/2016JA023205

Ulusen, D., Brain, D. A., and Mitchell, D. L. (2011). Observation of conical electron distributions over Martian crustal magnetic fields. *J. Geophys. Res.: Space Phys.*, *116*(A7), A07214. https://doi.org/10.1029/2010JA016217

Verigin, M. I., Gringauz, K. I., Shutte, N. M., Haider, S. A., Szego, K., Kiraly, P., Nagy, A. F., and Gombosi, T. I. (1991). On the possible source of the ionization in the nighttime Martian ionosphere. 1. Phobos 2 HARP electron spectrometer measurements. *J. Geophys. Res.: Space Phys.*, *96*(A11), 19307–19313. https://doi.org/10.1029/91JA00924

Weber, T., Brain, D., Mitchell, D., Xu, S. S., Connerney, J., and Halekas, J. (2017). Characterization of low-altitude nightside Martian magnetic topology using electron pitch angle distributions. *J. Geophys. Res.: Space Phys.*, *122*(10), 9777–9789. https://doi.org/10.1002/2017JA024491

Wu, X. S., Cui, J., Cao, Y. T., Liu, L. J., Zhou, Z. J., Huang, Y. Y., He, F., and Wei, Y. (2019a). On the hardness of the photoelectron energy spectrum near mars. *J. Geophys. Res.: Planets*, *124*(11), 2745–2753. https://doi.org/10.1029/2019JE006093

Wu, X. S., Cui, J., Xu, S. S., Lillis, R. J., Yelle, R. V., Edberg, N. J. T., Vigren, E., Rong, Z. J., Fan, K., … Mitchell, D. L. (2019b). The morphology of the topside Martian ionosphere: implications on bulk ion flow. *J. Geophys. Res.: Planets*, *124*(3), 734–751. https://doi.org/10.1029/2018JE005895

Wu, X. S., Cui, J., Cao, Y. T., Sun, W. Q., Luo, Q., and Ni, B. B. (2020a). Response of photoelectron peaks in the Martian ionosphere to solar EUV/X-ray irradiance. *Earth Planet. Phys.*, *4*(4), 1–6. https://doi.org/10.26464/epp2020035

Wu, X. S., Cui, J., Yelle, R. V., Cao, Y. T., He, Z. G., He, F., and Wei, Y. (2020b). Photoelectrons as a tracer of planetary atmospheric composition: Application to CO on Mars. *J. Geophys. Res.: Planets*, *125*(7), e2020JE006441. https://doi.org/10.1029/2020JE006441

Xu, S. S., Liemohn, M., Bougher, S., and Mitchell, D. (2015). Enhanced carbon dioxide causing the dust storm-related increase in high-altitude photoelectron fluxes at Mars. *Geophys. Res. Lett.*, *42*(22), 9702–9710. https://doi.org/10.1002/2015GL066043

Xu, S. S., Liemohn, M., Bougher, S., and Mitchell, D. (2016a). Martian high-altitude photoelectrons independent of solar zenith angle. *J. Geophys. Res.: Space Phys.*, *121*(4), 3767–3780. https://doi.org/10.1002/2015JA022149

Xu, S. S., Mitchell, D., Liemohn, M., Dong, C. F., Bougher, S., Fillingim, M., Lillis, R., Mcfadden, J., Mazelle, C., … Jakosky, B. (2016b). Deep nightside photoelectron observations by MAVEN SWEA: Implications for Martian northern hemispheric magnetic topology and nightside ionosphere source. *Geophys. Res. Lett.*, *43*(17), 8876–8884. https://doi.org/10.1002/2016GL070527

Xu, S. S., Mitchell, D., Liemohn, M., Fang, X. H., Ma, Y. J., Luhmann, J., Brain, D., Steckiewicz, M., Mazelle, C., … Jakosky, B. (2017a). Martian low-altitude magnetic topology deduced from MAVEN/SWEA observations. *J. Geophys. Res.: Space Phys.*, *122*(2), 1831–1852. https://doi.org/10.1002/2016JA023467

Xu, S. S., Mitchell, D., Luhmann, J., Ma, Y. J., Fang, X. H., Harada, Y., Hara, T., Brain, D., Weber, T., … DiBraccio, G. A. (2017b). High-altitude closed magnetic loops at mars observed by MAVEN. *Geophys. Res. Lett.*, *44*(22), 11229–11238. https://doi.org/10.1002/2017GL075831

Xu, S. S., Weber, T., Mitchell, D. L., Brain, D. A., Mazelle, C., DiBraccio, G. A., and Espley, J. (2019). A technique to infer magnetic topology at mars and its application to the terminator region. *J. Geophys. Res.: Space Phys.*, *124*(3), 1823–1842. https://doi.org/10.1029/2018JA026366